



Magnetic anisotropy in square pyramidal cobalt(II) complexes supported by tetraazomacrocyclic ligand

| | |
|-------------------------------|--|
| Journal: | <i>Dalton Transactions</i> |
| Manuscript ID | DT-ART-06-2020-001954.R2 |
| Article Type: | Paper |
| Date Submitted by the Author: | 03-Sep-2020 |
| Complete List of Authors: | <p>Cui, Hui-Hui; Coordination Chemistry Institute, State Key Laboratory of Coordination Chemistry Ding, Man-Man; Nanjing Normal University, School of Physical Science and Technology, Zhang, Xiu-Du; Anhui Normal University, College of Chemistry and Materials Science Lv, Wei; Coordination Chemistry Institute, State Key Laboratory of Coordination Chemistry Zhang, Yi-Quan; School of Physical Science and Technology, Physical department Chen, Xue-tai; Coordination Chemistry Institute, State Key Laboratory of Coordination Chemistry; Wang, Zhenxing; Huazhong University of Science and Technology, Wuhan National High Magnetic Field Center; Ouyang, Zhongwen; National High Magnetic Field Center, Huazhong University of Science and Technology, Xue, Zi-Ling; University of Tennessee, Department of Chemistry</p> |
| | |



Journal Name

ARTICLE

Magnetic anisotropy in square pyramidal cobalt(II) complexes supported by a tetraazomacrocyclic ligand

Received 00th January 20xx,
Accepted 00th January 20xx

Hui-Hui Cui,^a Man-Man Ding,^b Xiu-Du Zhang,^c Wei Lv,^a Yi-Quan Zhang,^{*b} Xue-Tai Chen,^{*a} Zhenxing Wang,^{*d} Zhong-Wen Ouyang,^d and Zi-Ling Xue^e

DOI: 10.1039/x0xx00000x

www.rsc.org/

Two five-coordinate mononuclear Co(II) complexes [Co(12-TMC)X][B(C₆H₅)₄] (L = 1, 4, 7, 10-tetramethyl-1, 4, 7, 10-tetraazacyclododecane (12-TMC), X = Cl⁻ (**1**), Br⁻ (**2**)) have been studied by X-ray single crystallography, magnetic measurements, high-frequency and -field EPR (HF-EPR) spectroscopy and theoretical calculations. Both complexes have a distorted square pyramidal geometry with the Co(II) ion lying above the basal plane constrained by the rigid tetradentate macrocyclic ligand. In contrast with the reported five-coordinate Co(II) complex [Co(12-TMC)(NCO)][B(C₆H₅)₄] (**3**) exhibiting easy-axis anisotropy, an easy-plane magnetic anisotropy were found for **1** and **2** via the analyses of the direct-current magnetic data and HF-EPR spectroscopy. Frequency- and temperature-dependent alternating-current magnetic susceptibility measurements demonstrated that complexes **1** and **2** show slow magnetic relaxation at an applied dc field. *Ab initio* calculations have been performed to reveal the impact of the terminal ligands on the nature of magnetic anisotropies of this series of five-coordinate Co(II) complexes.

Introduction

Single-molecule magnets (SMMs),¹⁻³ which display slow magnetic relaxation at low temperature, have been the recent hot topics of molecular magnetism due to their potential applications such as molecular spintronics, ultra-dense information storage and quantum computing.⁴⁻⁶ Thermal energy barrier (*U*) for the reversal of magnetic moment in a SMM is usually governed by the total spin (*S*) and easy axis anisotropy parameter (*D*), which can be defined as $|D|S^2$ and $|D|(S^2 - 1/4)$ for integer and half-integer spins, respectively.¹ Since polynuclear transition metal clusters with a large spin (*S*) ground state will not exhibit superior properties, a substantial effort has been devoted to those SMMs containing one paramagnetic lanthanide⁷⁻⁸ and transition-metal ion,⁹⁻¹² which are termed as single-ion magnets (SIMs). They are the simplest systems,

in which magnetic anisotropy and magnetic dynamics can be fine-tuned via variation of the ligand field around the metal center.

To date a large number of SIMs based on the first row transition metal complexes have been reported.⁹⁻¹² Among the 3d-SIMs, the anisotropic Co(II) complexes are most extensively studied due to the non-integer spin ground state, which decreases the probability of quantum tunnelling of magnetization (QTM).¹³ So far various Co(II)-based SIMs with different coordination geometries and environments are known. Compared to the large number of examples of four- and six-coordinate analogues,^{9-12,14-19} the number of five-coordinate Co(II)-SIMs is relatively limited.²⁰⁻⁵⁷ The reported five-coordinate Co(II)-SIMs are summarized in Tables S1 and S2 (ESI[†]) along with their structural features and magnetic parameters. We have collected or calculated Addison τ^5 value⁵⁸ and the continuous shape measure (*CSHM*) values⁵⁹⁻⁶⁰ to evaluate the degree of deviation from the ideal square pyramidal and trigonal bipyramidal symmetries when the values were not reported in the literature. The τ^5 value is zero for an ideal square pyramid, while a value of 1 corresponds to the ideal trigonal bipyramidal configuration.⁵⁸ The most well-known family are those with the molecular formula [(NNN)CoX₂] (X = halide or pseudohalide) supported by tridentate nitrogen ligands (NNN) together with two halido or pseudohalido ligands (Table S1, ESI[†]).²⁰⁻³⁵ Their reported τ^5 values vary in a wide range from 0.01 to 0.83, meaning that the coordination geometries could be distorted square pyramid and trigonal bipyramid with various distortion degrees. It is found that their coordination geometries change with the tridentate NNN ligand and/or the terminal ligand. For example, the configuration of [Co(terpy)Cl₂] ($\tau^5 = 0.05$) is a distorted square pyramidal geometry while the Co(II) coordination geometry in [Co(terpy)(NCS)₂] shifts towards trigonal bipyramid ($\tau^5 = 0.43$).²⁰ Similarly, halido or pseudohalido ligand has a significant impact on the geometry of the metal coordination sphere of five-coordinate Co(II) complexes with

^a State Key Laboratory of Coordination Chemistry, School of Chemistry and Chemical Engineering, Nanjing University, Nanjing 210023, China. E-mail: xtchen@nju.edu.cn

^b Jiangsu Key Laboratory for NSLSCS, School of Physical Science and Technology, Nanjing Normal University, Nanjing 210023, China

^c College of Chemistry and Materials Science, Anhui Normal University, 189 Jiu Hua Southern Road, Wuhu, China

^d Wuhan National High Magnetic Field Center & School of Physics, Huazhong University of Science and Technology, Wuhan 430074, China

^e Department of Chemistry, University of Tennessee, Knoxville, Tennessee 37996, USA.

[†] Electronic supplementary information (ESI) available: Tables for the summary of the reported five-coordinate Co(II)-SIMs; Table for the calculations by SHAPE; Table for the fitting data for the Cole-Cole plot; Tables for the theoretical calculation data; Figures of XRD patterns for **1-2**; Additional figures for magnetic characterization, HF-EPR data and theoretical calculations; Additional structural data in CIF format (CIF). See DOI: 10.1039/x0xx00000x

bis(imino)pyridine pincer ligands (Table S1, ESI[†]) with the τ^5 values in a range of 0.03–0.43.^{22–24} Furthermore, the substituent in the tridentate nitrogen ligand also influences the coordination geometry. [Co(L^{2a})(NCS)₂], for example, has a larger τ^5 value (0.27) than [Co(L^{2b})(NCS)₂] (0.03) (Entries 4 and 5, Table S1 and Scheme S1, ESI[†]).²² This change in coordination geometry complicates the studies of the influence of the terminal ligand on magnetic properties. A more stable configuration towards the terminal ligand is desired. A rigid tetradentate tripodal ligand favours trigonal bipyramidal configuration, in which a terminal ligand can be varied. For the trigonal bipyramidal Co(II) complexes supported by the tripodal tetradentate ligands L⁹–L¹⁴ (Table S2, Scheme 2, ESI[†]), whose Addison parameters τ^5 range from 0.83 to 1.0.^{19–29} The magnetic anisotropy is negative when the terminal ligand is halide or pseudohalide such as NCS. However, positive anisotropy is found when the terminal ligand is neutral, such as H₂O or CH₃CN for L¹⁰ or L¹³ as the supporting ligand.^{38,45} Similar systematic studies have not been performed for the square pyramidal Co(II)-SIMs yet.

In view of the above-mentioned background, a rigid tetradentate macrocyclic ligand 1, 4, 7, 10-tetramethyl-1, 4, 7, 10-tetraazacyclododecane (12-TMC)⁶¹ has attracted our attention. The rigidity of tetradentate macrocyclic backbone meets the requirement for obtention of the isostructural square pyramidal configuration. In 2017, we have employed 12-TMC to synthesize five-coordinate Co(II) complexes [(12-TMC)Co(CH₃CN)]²⁺ with CH₃CN as the axial ligand, which display spin-crossover with incomplete transition and low-temperature, field-induced SIM behaviour originating from the low spin state of Co(II).⁵⁶ Subsequently, a high-spin square pyramidal Co(II) complex [Co(12-TMC)(NCO)][B(C₆H₅)₄] (3) with NCO[−] as the axial ligand demonstrated an easy-axial magnetic anisotropy and field-induced slow magnetic relaxation.⁵⁷ These studies clearly show that the variation of the axial ligand could tune the electronic structure and the magnetic anisotropy. Herein we present the synthesis and structures of square pyramidal 12-TMC-Co(II) compounds [Co(12-TMC)X][B(C₆H₅)₄] with Cl[−] (1) or Br[−] (2) in the axial position. By analysing the direct-current (dc) magnetic data, 1 and 2 are found to exhibit easy-plane magnetic anisotropy with the similar *D* values of +44.43 and +52.06 cm^{−1}. The easy-plane anisotropic nature has been confirmed by high-field and high-frequency electron paramagnetic resonance (HF-EPR) spectroscopy and theoretical calculations. Alternating-current (ac) magnetic susceptibility measurements demonstrated the field-induced slow magnetization relaxation in 1 and 2.

Experimental

Synthesis and general characterization

The reactions were carried out using standard Schlenk techniques under N₂ atmosphere. All the solvents were dried and purified using conventional methods before use. The other chemicals employed were commercially available and used as received. Tetrphenylboron silver (Ag[B(C₆H₅)₄]) was synthesized from AgNO₃ and Na[B(C₆H₅)₄] in water. 1, 4, 7, 10-Tetramethyl-1, 4, 7, 10-tetraazacyclododecane (12-TMC) was prepared by the literature procedure.⁶¹ Elemental analyses were performed on an Elementar Vario ELIII elemental analyser. Powder X-ray diffraction (PXRD) patterns were recorded on a Bruker D8 ADVANCE X-ray powder diffractometer with a Cu K α X-ray source ($\lambda = 1.54056 \text{ \AA}$) operated at 40 kV and 40 mA.

Synthesis of 1 and 2

Co(12-TMC)Cl][B(C₆H₅)₄] (1). CoCl₂ (0.5 mmol, 0.065 g) and 12-TMC (1.0 mmol, 0.19 g) were dissolved in 15 mL of CH₃CN and stirred at room temperature for 6 h to give a blue solution. Ag[B(C₆H₅)₄] (0.5 mmol, 0.214 g) was added to the solution and stirred for another 3 h and then filtrated. The diffusion of diethyl ether into the acetonitrile solution in one week gave the blue crystals of **1** at 70% yield based on Co. Anal. Calc. for C₃₆H₄₈BCoN₄Cl: C, 67.35; H, 7.54; N, 8.73. Found: C, 67.40; H, 7.49; N, 8.69.

[Co(12-TMC)Br][B(C₆H₅)₄] (2). **2** was synthesized by the same procedure as **1**, but using CoBr₂ (0.5 mmol, 0.11 g) instead of CoCl₂ (0.5 mmol, 0.065 g). The blue crystals of **2** formed with a yield of 65% based on Co. Anal. Calc. for C₃₆H₄₈BCoN₄Br: C, 62.99; H, 7.05; N, 8.16. Found: C, 62.93; H, 6.96; N, 8.22.

X-ray single-crystal structure determination

Single-crystal X-ray crystallographic data were collected for **1** and **2** using a Bruker APEX DUO diffractometer at 155 K with a CCD area detector (Mo K α radiation, $\lambda = 0.71073 \text{ \AA}$).⁶² The APEXII program was used for collecting frames of data and determining the unit cell parameters. The data were integrated with SAINT program⁶³ and corrected for Lorentz factor and polarization effects. The absorption corrections were applied using SADABS.⁶⁴ The molecular structures were solved and completed via full-matrix least-squares procedure SHELXL (version 2014/7).⁶⁵ The Co atom was determined first using the difference Fourier maps and then the other non-hydrogen atoms were subsequently identified. All non-hydrogen atoms were refined anisotropically and hydrogen atoms were set and generated as riding on the corresponding non-hydrogen atoms.

Magnetic measurements

Magnetic measurements were performed using a vibrating sample magnetometer (VSM) of Quantum Design MPMS SQUID-VSM system, with ground microcrystalline powders which were restrained in a frozen eicosane matrix and tightly packed in a polycarbonate plastic capsule to prevent torquing of crystallites under magnetic field. Variable temperature direct-current susceptibility data of **1** and **2** were collected under a field of 0.10 T in the range of 2–300 K. The field-dependent magnetizations were measured in the range of 1–7 T at 1.8 K, 3.0 K and 5.0 K. Alternating-current (ac) susceptibility measurements were carried out with an oscillating ac field of 2 Oe at frequencies ranging from 1 to 1000 Hz under different external fields. All magnetic susceptibilities data were corrected for the diamagnetic contributions of sample holder as well as for diamagnetism of the sample using Pascal's constants.⁶⁶

HF-EPR measurements.

HF-EPR spectra were recorded on a locally developed spectrometer at the Wuhan National High Magnetic Field Center, China.^{67–68} The microwaves of the transmission-type instrument are propagated by over-sized cylindrical light pipes. The samples were measured with KBr and pressed into pellets to minimize the effect of field-induced torquing.

Results and discussion

Synthesis

Complexes **1** and **2** were prepared similarly by direct mixing of the 12-TMC and CoX_2 ($\text{X} = \text{Cl}, \text{Br}$) in CH_3CN . A blue solution was developed and then treated with one equiv of $\text{Ag}[\text{B}(\text{C}_6\text{H}_5)_4]$ to give a solution containing the desired product and the precipitation of AgX ($\text{X} = \text{Cl}, \text{Br}$). The crystalline product was obtained by diethyl ether vapor diffusion into the CH_3CN solution in a good yield. The phase purity of samples of **1** and **2** were confirmed by PXRD spectra and elemental analysis (Fig. S1-S2, ESI[†]).

Crystal structural descriptions

The crystallographic data and the parameters of single crystal structural analyses are listed in Table S3[†]. The selected bond parameters of **1-2** are shown in Table S4[†]. Compounds **1-2** crystallize in the same monoclinic space group $P2_1/c$. The asymmetric units of **1** and **2** contain two crystallographically different molecules **1a**, **1b**, **2a** and **2b** (Fig. 1 and Fig. S3, ESI[†]). The structural parameters of two distinct molecules in **1** and **2** vary only slightly. As shown in Fig. 1, the cation is five-coordinate with a square pyramidal configuration, in which a central $\text{Co}(\text{II})$ ion is coordinated by four nitrogen atoms of 12-TMC ligand in equatorial positions, and a halide ion in an axial position. The important structural parameters of **1** and **2** and the reported $[\text{Co}(\text{TMC})(\text{NCO})][\text{B}(\text{C}_6\text{H}_5)_4]$ (**3**)⁵⁷ are listed in Table 1 for comparison. The average $\text{Co}-\text{N}_{\text{eq}}$ bond lengths are 2.1544, 2.1567, 2.1578 and 2.1603 Å for **1a**, **1b**, **2a** and **2b**, respectively, and they are similar to 2.1608 Å reported for **3**.⁵⁷ The $\text{Co}-\text{X}$ bond distances in an axial position are much longer than $\text{Co}-\text{N}$ in the equatorial position. The $\text{Co}-\text{Cl}$ bonds of 2.2425(8) Å for **1a**, 2.2267(7) Å for **1b** are shorter than $\text{Co}-\text{Br}$ bonds of 2.4017(10) Å for **2a**, 2.3641(8) Å for **2b**, which is in accord with the different ionic radius of the corresponding halide ion. These $\text{Co}-\text{X}_{\text{axial}}$ bonds in **1** and **2** are longer than the $\text{Co}-\text{N}_{\text{axial}}$ bond in **3** (1.9399(17) Å).⁵⁷ The metal center is located out of the basal N_4 plane by 0.807 Å (**1a**), 0.811 Å (**1b**), 0.810 Å (**2a**), and 0.817 Å (**2b**), similar to 0.802 Å in **3**.⁵⁷ The bond angles between the two neighboring nitrogen atoms around $\text{Co}(\text{II})$ ion are in the range of 81.19(8)°–82.66(9)° for **1-2**. The $\text{N}-\text{Co}-\text{N}$ bond angles with the two opposite nitrogen atoms are in the range of 134.87(15)°–136.78(8)°, which are much smaller than 180°. These bond angles are also comparable to those in **3**.⁵⁷ The shortest intermolecular $\text{Co}\cdots\text{Co}$ distances are 6.238 Å for **1** and 6.528 Å for **2**, respectively.

The calculated τ^5 values, defined as an index of the distortion degree between trigonal bipyramidal and square pyramidal configurations, are 0.027, 0.023, 0.019, 0.024 for **1a**, **1b**, **2a** and **2b**, similar to that of **3** (0.012), indicating that the coordination geometry at the $\text{Co}(\text{II})$ centre can be described as slightly distorted square pyramid.⁵⁸ Furthermore, the continuous shape measure (*CShM*) analyses were calculated by SHAPE 2.1⁵⁹⁻⁶⁰ to evaluate the degree of deviation from the ideal square pyramidal and trigonal bipyramidal symmetries. The distortion values of **1-2** confirm that they can be described as square pyramid (0.759 for **1a**, 0.760 for **1b**, 1.124 for **2a**, and 1.081 for **2b**) rather than as trigonal bipyramid (5.624 for **1a**, 5.640 for **1b**, 5.983 for **2a**, and 5.857 for **2b**, Table S5, ESI[†]). The above structural parameters show the stability of the square pyramidal configuration in this series of five-coordinate $\text{Co}(\text{II})$ complexes. The most significant distinction between **1**, **2** and **3** is the axial ligand – weak halide ligand (**1** and **2**) vs stronger NCO^-

ligand (**3**), and the distinction may be responsible for the different magnetic anisotropy.

There are significant weak interactions in the crystal structures of **1** and **2**. Weak $\text{C}-\text{H}\cdots\text{X}-\text{M}$ hydrogen bonds are found in molecule **1b** containing $\text{Co}2$ between the coordinated chlorine atom and one hydrogen atom of TMC from adjacent **1b** molecules ($\text{H}\cdots\text{Cl} = 2.654$ Å) to form one-dimensional hydrogen-bonded chain (Fig. S4a, ESI[†]). Around these chains, the BPh_4^- anions based on B1 atoms are assembled through the $\text{C}-\text{H}\cdots\pi$ interactions (2.883 Å) to generate one-dimensional binary supramolecular chains (Fig. S4a, ESI[†]). Every two adjacent molecules of **1a** containing $\text{Co}1$ form a dimer through $\text{C}-\text{H}\cdots\text{Cl}$ ($\text{H}\cdots\text{Cl} = 2.853$ Å), which further join the binary chains to give two-dimensional supramolecular layers via the hydrogen bonds ($\text{H}\cdots\text{Cl} = 2.776$ Å) between the chlorine atom (Cl1) and BPh_4^- anions based on B1 atoms (Fig. S4b, ESI[†]). Significant $\text{C}-\text{H}\cdots\pi$ and $\pi\cdots\pi$ (T -shaped) interactions between the BPh_4^- anions based on B2 atoms and the neighbouring layers promote the formation of three-dimensional structure (Fig. S4c, ESI[†]). Similar supramolecular interactions exist in the crystal structure of **2** (Fig. S5, ESI[†]).

Table 1. Important structural parameters of **1-3**.

| | 1a | 1b | 2a | 2b | 3^c |
|--|-----------|-----------|-----------|-----------|----------------------|
| av. $\text{Co}-\text{N}$ (Å) | 2.1544 | 2.1567 | 2.1578 | 2.1603 | 2.1608 |
| av. $\text{Co}-\text{X}$ (Å) | 2.2425 | 2.2267 | 2.4017 | 2.3641 | 1.9399 |
| av. <i>cis</i> - $\text{N}-\text{Co}-\text{N}$ (°) | 81.93 | 81.87 | 81.88 | 82.17 | 82.09 |
| <i>trans</i> - $\text{N}-\text{Co}-\text{N}$ (°) | 136.98 | 135.81 | 135.83 | 135.58 | 136.36 |
| d (Å) ^a | 0.807 | 0.811 | 0.810 | 0.817 | 0.802 |
| τ^5 | 0.027 | 0.023 | 0.019 | 0.024 | 0.012 |
| <i>CShM</i> (4py) | 0.759 | 0.760 | 1.124 | 1.081 | 0.442 |
| $\text{Co}\cdots\text{Co}$ (Å) ^b | 6.238 | | 6.528 | | 7.094 |

a. The distance of $\text{Co}(\text{II})$ ion lying out of the basal N_4 plane; b. The shortest intermolecular $\text{Co}\cdots\text{Co}$ distance; c. Reference 57.

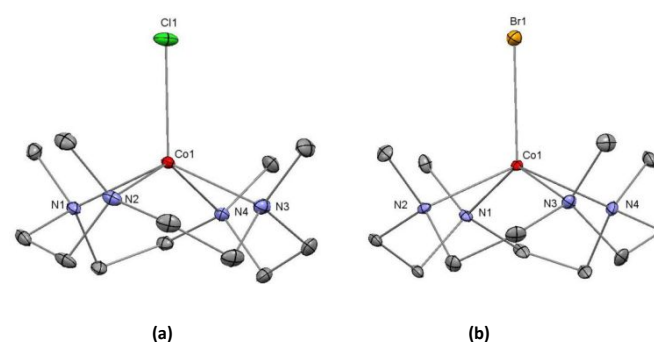


Fig. 1 Structure of the anion of (a) **1a** and (b) **2a**. Red, blue, green, orange and gray spheres represent Co, N, Cl, Br and C atoms. H atoms are omitted for clarity.

Static magnetic properties

Variable-temperature direct-current (dc) magnetic susceptibilities were measured on polycrystalline samples of **1-2** in the temperature range of 2–300 K under an applied field of 0.10 T. As shown in Fig. 2 and S6[†], the resulting $\chi_{\text{M}}T$ versus T curves show the similar trend. At room temperature, the $\chi_{\text{M}}T$ values are 3.03, and 3.15 K mol^{-1} for **1** and **2**, respectively. These are considerably larger than the spin-only value of 1.875 $\text{cm}^3 \text{mol}^{-1} \text{K}$ for a high-spin $\text{Co}(\text{II})$

ion ($S = 3/2$, $g = 2.0$), which can be attributed to the significant orbital contribution. Upon cooling from 300 K, the $\chi_M T$ values decrease slowly until 75 K, below which, they fall abruptly and reach 1.84 and 1.99 $\text{cm}^3 \text{mol}^{-1} \text{K}$ at 2 K for **1** and **2**, respectively. This decline at the low temperature range should be, to a great extent, due to the intrinsic magnetic anisotropy of the Co(II) ion.

The field-dependent magnetizations were collected at applied magnetic fields in a range of 1-7 T below 5 K (Fig. 2 and S6, ESI[†]). The magnetization values are 2.47 and 2.60 $N\mu_B$ for **1** and **2** at 7 T, without reaching saturation. The lack of saturation agrees with the presence of magnetic anisotropy.

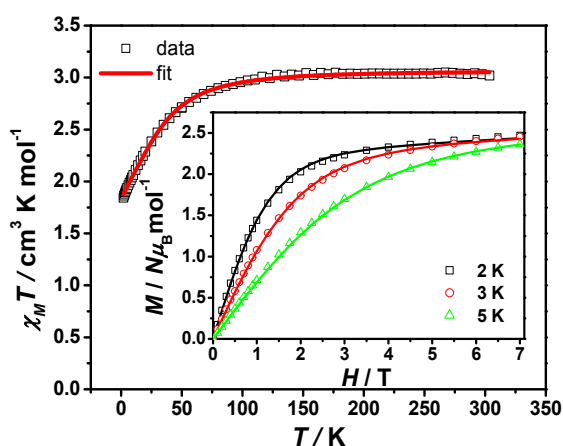


Fig. 2 Variable-temperature dc susceptibility data of **1** under 0.10 T applied dc field. Inset: field dependence of the magnetization below 5 K for **1**. Solid lines are the fits to the data with program PHI.⁶⁹

As in most of Co(II) complexes, the static magnetic data of five-coordinate Co(II) complexes were usually modelled by the conventional spin-Hamiltonian based on the assumption that the zero-field splitting (ZFS) parameters, axial D and rhombic E , can be used to present their magnetic anisotropy. Our theoretical calculations have showed that their anisotropies of **1-2** can be approximately depicted by the effective spin Hamiltonian with zero-field splitting parameters D and E (vide infra). Therefore, the $\chi_M T$ versus T and M versus H curves were fit simultaneously with the following spin Hamiltonian (equation 1) employing the PHI program,⁶⁹

$$H = D(\hat{S}_z^2 - S(S+1)/3) + E(\hat{S}_x^2 - \hat{S}_y^2) + \mu_B g \hat{S} \cdot H \quad (1)$$

where μ_B is the Bohr magneton, g is a tensor, H is the magnetic field vector. In addition, the intermolecular exchange interactions with zJ parameter was considered. The resulting parameters including D and E values are afforded in Table 2. As we can see, the signs of ZFS parameters D are positive with the values of +44.43(9) and +52.06(2) cm^{-1} for **1** and **2**, respectively, implying the significant easy-plane anisotropy. This positive sign of D value was further confirmed by the fact that the fitting could not give the reasonable agreement when the D value was set negative.

Table 2. The spin-Hamiltonian parameters of **1-2** obtained by the fitting of magnetic data.

| | 1 | 2 |
|--|----------|----------|
|--|----------|----------|

| | | |
|---------------------------|------------|-----------|
| D , cm^{-1} | + 44.43(7) | +52.06(2) |
| E , cm^{-1} | -2.27(0) | 0.014(2) |
| g_{xy} | 2.62(2) | 2.75(1) |
| g_z | 2.37(5) | 2.16(7) |
| zJ (cm^{-1}) | -0.014(7) | -0.032(7) |

HF-EPR spectroscopy

It is well known that the reliability of the magnetic parameters from the fitting of static magnetic data, especially the sign of the magnetic anisotropy derived, may be questioned. In order to get further insight into the magnetic anisotropy, especially confirming the positive sign of D parameter, HF-EPR spectra were recorded for the polycrystalline samples of **1** and **2**. Although there are two crystallographically different molecules in the crystal lattice of **1**, only one set of EPR features were observed (Fig. 3a). In contrast, two sets of three EPR features were found for **2** in accordance with the two crystallographically different molecules (Fig. S7, ESI[†]). This implies that the EPR responses of the two crystallographically different molecules are similar and overlapped in **1** due to the same $CS_{\text{eff}}M$ values (0.759 for **1a** and 0.760 for **1b**), but are distinct in **2** with rather significantly different $CS_{\text{eff}}M$ values (1.124 for **2a** and 1.081 for **2b**). The resonance fields at various microwave frequencies are extracted and plotted in Fig. 3b and S7b[†], in which three straight lines are obtained, corresponding to each set of the three features. This suggests that the separation of the Kramers doublets [$2(D^2 + 3E^2)^{1/2}$] is larger than quantum energy of the microwave frequency. Only the Kramers doublet would be populated at low temperature and the observed resonances are attributed to the intra-Kramers transitions within the lowest doublet $M_S = \pm 1/2$ with $\Delta M_S = \pm 1$. These spectra can be interpreted in terms of an effective spin $S_{\text{eff}} = 1/2$ state and effective g values. The typical EPR at 219 GHz and 2D resonating field versus frequency map of **1** was fit by using SPIN⁷⁰ (Fig. S8, ESI[†]) to give the effective g values with $g_1' = 6.80$, $g_2' = 2.98$ and $g_3' = 1.66$, corresponding to an effective spin doublet ($S_{\text{eff}} = 1/2$), indicating the easy-plane magnetic anisotropy in **1**.⁷¹⁻⁷² The six signals observed in **2** preclude the definite assignment of each set of three features and the simulation, but the sign of D value is positive.

The HF-EPR data can be used to prove the positive sign of D value and estimate the $\lambda = E/D$ value according to the approach reported by Misochko et al.⁷³ It is known that the effective g_{eff} values with $S_{\text{eff}} = 1/2$ are related to the g values corresponding to the true spin $S = 3/2$ in equation 2.⁷²⁻⁷⁵

$$\begin{aligned} g_x' &= g_x \left(1 + \frac{1-3\lambda}{\sqrt{1+3\lambda^2}} \right) \\ g_y' &= g_y \left(1 + \frac{1+3\lambda}{\sqrt{1+3\lambda^2}} \right) \\ g_z' &= g_z \left(\frac{2}{\sqrt{1+3\lambda^2}} - 1 \right) \end{aligned} \quad (2)$$

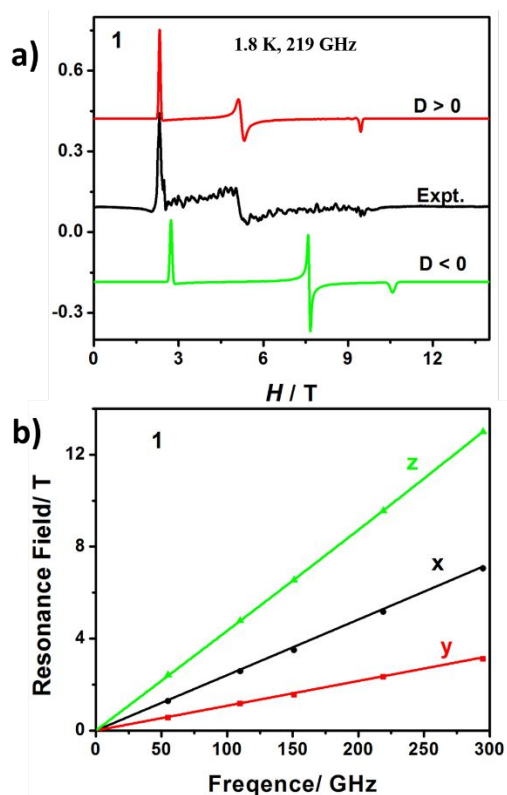


Fig. 3 a) Representative HFEPR spectrum of **1** at 1.8 K (black) with the simulations using spin Hamiltonian with the true spin $S = 3/2$ (red: $D > 0$; green: $D < 0$). b) Resonance field vs. microwave frequency for EPR transitions for **1** and the simulations with spin Hamiltonian with the true spin $S = 3/2$.

Since the experimentally determined g_1' , g_2' and g_3' values are not fully assigned to the principal axes in the above fitting with $S_{\text{eff}} = 1/2$ model, we have in principle to assign g_1' , g_2' and g_3' to g_x' , g_y' and g_z' in six possibilities: $(g_x', g_y', g_z') = (g_1', g_2', g_3')$ or (g_1', g_3', g_2') or (g_2', g_1', g_3') or (g_2', g_3', g_1') or (g_3', g_1', g_2') or (g_3', g_2', g_1') . For each assignment, with the known g_x' , g_y' and g_z' values, we can calculate the g values as a function of λ as shown in Fig. S9†. Considering that the g values of Co(II) complexes are in the range from 2 to 3,^{9,57,71-72} only one assignment $(g_x', g_y', g_z') = (g_2', g_1', g_3') = (2.98, 6.80, 1.66)$ is realistic (Fig. S9c, ESI†) and the other five assignments should not be considered further.

It has also been demonstrated that the g and λ values are not independent but related to each other with a relationship shown in equation 3.⁷⁵⁻⁷⁶

$$\lambda = \frac{g_x - g_y}{2g_z - (g_x + g_y)} \quad (3)$$

Following the approach of Misochko et al,⁷³ we define a function $f(\lambda)$ as shown in equation 4 in order to determine the λ value using the graph method.

$$f(\lambda) = \frac{g_x(\lambda) - g_y(\lambda)}{2g_z(\lambda) - [g_x(\lambda) + g_y(\lambda)]} - \lambda \quad (4)$$

We can draw a graph of function $f(\lambda)$, in which the λ value of 0.274 is found when $f(\lambda) = 0$ (Fig. 4). Subsequently $g_x = 2.567$, $g_y = 2.570$ and $g_z = 2.057$ can be calculated according to equation 2. With these g_x , g_y , g_z and λ values, the 2D resonating field versus

frequency map and the spectra of **1** (Fig. 3) were simulated using spin Hamiltonian with the true spin $S = 3/2$ shown in equation 1 assuming D value (+44.43 cm^{-1}) as that determined by magnetic data.⁷⁰ As shown in Fig. 3a, the simulated spectrum agrees well with experimental one, confirming that the sign of D value is positive rather than negative for **1** since no reasonably simulated spectrum could be obtained if the sign of D was assigned as negative.

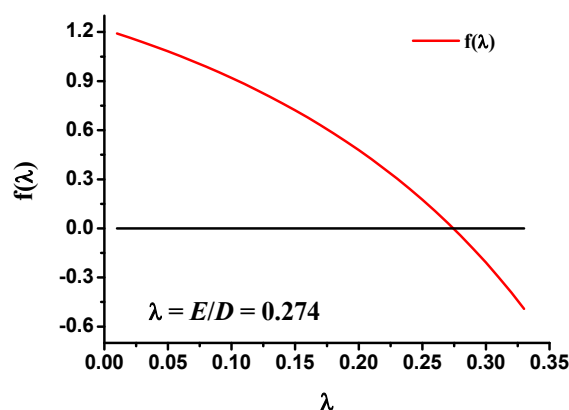


Fig. 4 Dependences $f(\lambda)$ plotted for the assignments of $(g_x', g_y', g_z') \leftrightarrow (g_2', g_1', g_3')$, yielding $\lambda = 0.274$ at $\gamma = 0$.

Dynamic magnetic properties

To investigate the relaxation dynamics, temperature- and frequency-dependent alternating-current (ac) susceptibility measurements were performed on polycrystalline samples of **1** and **2**. Under zero static magnetic field, there was no out-of-phase susceptibility signals. The field dependent measurements were performed under various dc fields up to 0.20 T at 1.8 K (Fig. S10, ESI†). Significant frequency-dependent out-of-phase signals (χ''_M) were observed for **1** and **2**, suggesting that **1** and **2** are field-induced single-ion magnets. The data indicate that the optimum fields to reduce the QTM effect are 0.08 and 0.10 T for **1** and **2**, respectively. Therefore, these optimum fields are used for the further temperature- and frequency-dependent ac measurements in the temperature range of 1.8–3 K (Fig. 5, S11 and S12, ESI†). The peaks of χ''_M signals for **1** and **2** appear at 389 Hz and 559 Hz at 1.8 K, respectively. With the increase of temperature, the peaks value of χ''_M shift gradually to the high frequency region.

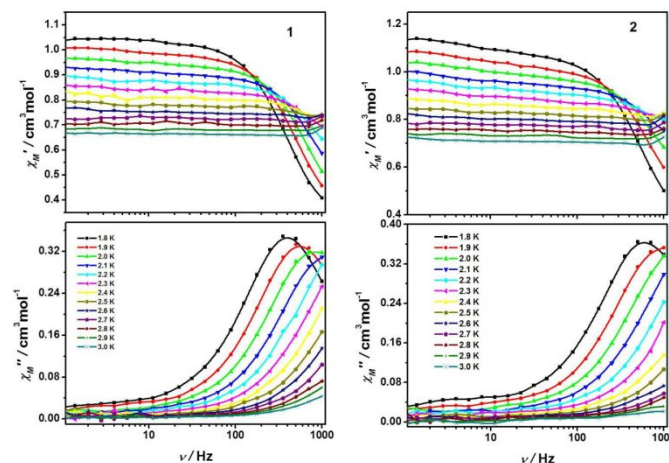


Fig. 5 Frequency dependence of the ac susceptibility from 1.8 to 3 K for **1-2**. The solid lines are for eye guide.

The Cole–Cole plots (Fig. 6a and S13, ESI[†]) generated from the alternating-current susceptibility data were fit using the generalized Debye model⁷⁷⁻⁷⁸ (equation 5) to extract the values and distribution of the relaxation times (Table S6, ESI[†])

$$\chi_{ac}(\omega) = \chi_S + \frac{\chi_T - \chi_S}{1 + (i\omega\tau)^{1-\alpha}} \quad (5)$$

where χ_T and χ_S are the isothermal and the adiabatic susceptibility, respectively; ω is angular frequency; τ is the relaxation time; α indicates the deviation from a pure Debye model.⁷⁷⁻⁷⁸ The obtained α values for **1** and **2** are in the range of 0.05–0.16 and 0.21–0.26 (Table S6, ESI[†]), respectively, which suggest the relatively narrow distribution of the relaxation times for **1** and a moderate distribution for **2**. The plots of $\ln(\tau)$ versus T^{-1} were modelled by using Raman process with the power law $\tau^{-1} = CT^n$, yielding $C = 31.61(5) \text{ s}^{-1} \text{ K}^{-7.45}$, $n = 7.45(7)$ for **1** and $C = 29.83(8) \text{ s}^{-1} \text{ K}^{-8.58}$, $n = 8.58(8)$ for **2** (Fig. 6b and S14, ESI[†]). The simulated data are in good agreement with the experimental ones and the values of n (7.45 for **1** and 8.58 for **2**) is approximately equal to 9, suggesting that Raman processes are dominating in both **1** and **2**. The fittings employing the Orbach and/or direct process could not give reasonable results. It is important to note that the extracted values from the above fits should be carefully considered since there are only few data points in a narrow temperature range (1.8 K–2.6 K). However, the above observations imply the similarity of magnetic dynamics of **1** and **2**.

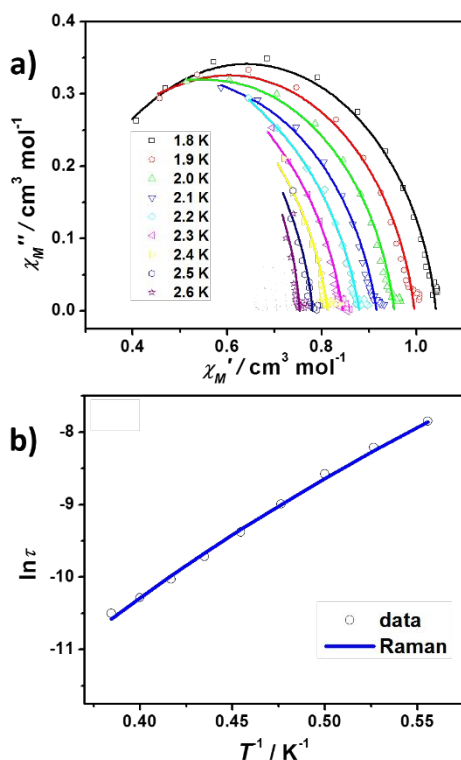


Fig. 6 a) Cole–Cole plots for **1** under 0.08 T dc field. The solid lines are the best fits to the experiments with the generalized Debye model. b) The plot of $\ln(\tau)$ versus T^{-1} for **1**. The solid red line represents the best fit by the Raman process.

In order to investigate the influence of dipolar interactions on the magnetic relaxation dynamics, magnetically diluted samples in

the diamagnetic Zn(II) matrix, $[\text{Co}_{0.1}\text{Zn}_{0.9}(\text{12-TMC})\text{Cl}][\text{B}(\text{C}_6\text{H}_5)_4]$ (**1'**) and $[\text{Co}_{0.1}\text{Zn}_{0.9}(\text{12-TMC})\text{Br}][\text{B}(\text{C}_6\text{H}_5)_4]$ (**2'**) were obtained via co-preparation starting with a 1:9 stoichiometry of Co(II) and Zn(II) salts. The diamagnetic Zn(II) analogs were also prepared and their single-crystal X-ray crystallographic data were collected. Unfortunately, only poor quality data were obtained, but the atom connectivity was definitely determined. The Zn(II) analogs exhibit the same crystalline phase with **1** and **2** (Fig. S15–S16, ESI[†]), which permits the facile preparation of the diluted samples. The resulting XRD (Fig. S17, ESI[†]) and ICP data confirmed that the diluted samples were successfully synthesized. Alternating-current (ac) susceptibility measurements showed that no ac susceptibility signal was observed for both complexes **1'** and **2'** under zero static field (Fig. S18, ESI[†]). Dc fields of 0.08 T and 0.10 T were applied during the ac measurement for **1'** and **2'**, respectively (Fig. S19–S22, ESI[†]). Upon dilution in the diamagnetic Zn(II) matrix, an obvious shift in χ_M'' to lower frequencies was observed for both **1'** and **2'**. Under the same applied dc field, the magnetic relaxation of diluted samples was relatively slower. To extract the values and distribution of the relaxation times, the Cole–Cole plots (Fig. S23, ESI[†]) were constructed by fitting of the χ_M'' vs χ_M' data with generalized Debye model,⁷⁷⁻⁷⁸ affording the α parameters in the range of 0.86×10^{-14} –0.08 for **1'** and 0.002–0.07 for **2'** (Table S7, ESI[†]). The relaxation times derived from the Cole–Cole plots were analyzed by using Raman mechanism for **1'** and **2'** (Fig. S24, ESI[†]). The fittings gave the following parameters of $C = 4.84(8) \text{ s}^{-1} \text{ K}^{-8.73}$, $n = 8.73(7)$ for **1'** and $C = 5.81(7) \text{ s}^{-1} \text{ K}^{-8.39}$, $n = 8.39(7)$ for **2'**. Compared with **1** and **2**, the relaxation times of diluted samples are obviously slower (Fig. S25, ESI[†]). The ac susceptibilities in diluted samples confirm that the slow magnetic relaxation originates from the individual complexes **1** and **2**.

Theoretical calculations

Ab initio multireference calculations were performed on **1** and **2** by CASPT2 with MOLCAS 8.4⁷⁹ and NEVPT2 with ORCA 4.2.⁸⁰ The calculations by CASPT2 have been performed for **3** and reported earlier.⁵⁷ Complex **3** has been further studied by NEVPT2 with ORCA 4.2, which are provided here for comparison. Calculation details are given in ESI[†].

The energies of the low-lying spin-free states and spin-orbit states were calculated for **1-3**, which are listed in Tables S8 and S9[†]. The energy gap between the two lowest spin-free states are larger than those between the lowest two spin-orbit states. Even though the compositions of the ground and first spin-orbit states of **1-3** are not formed from just the ground spin-free state, but the ground spin-state makes a major contribution with a percentage larger than 65% (Table S9, ESI[†]). In such cases, the effective spin-Hamiltonian with ZFS parameters D and E can be approximately used to depict their magnetic anisotropies.⁸¹⁻⁸² The ZFS parameters can be reasonably estimated. The calculated D , E (cm^{-1}) and g (g_x , g_y , g_z) tensors for **1-3** respectively, are listed in Table 3. The calculated positive D values (57.5, 56.1, 61.1 and 58.4 cm^{-1} for **1a**, **1b**, **2a**, and **2b** by CASPT2 method and 52.6, 52.0, 53.8 and 51.4 cm^{-1} for **1a**, **1b**, **2a** and **2b** by NEVPT2 calculations) show that **1** and **2** are easy-plane magnetic systems, while **3** is easy axial with a negative D value (–79.7 cm^{-1} by CASPT2 and –67.7 cm^{-1} by NEVPT2). These calculated results support the nature of magnetic anisotropies of **1-3** revealed

by magnetic and HF-EPR studies. With these computed parameters the $\chi_M T$ versus T plots of **1–3** were calculated as shown in Fig. S27†, which are in good agreement with the experimental ones.

Table 3. Calculated ZFS parameters D , E (cm^{-1}) and g (g_x , g_y , g_z) tensors of **1–3** using CASPT2 and NEVPT2 with MOLCAS 8.4 and ORCA 4.2, respectively.

| | CASPT2 | | | | |
|-----------|------------------|------------------|-------|-------|-------|
| | D_{cal} | E_{cal} | g_x | g_y | g_z |
| 1a | 57.5 | -7.9 | 3.086 | 2.943 | 1.829 |
| 1b | 56.1 | -5.8 | 2.968 | 2.859 | 1.915 |
| 2a | 61.1 | -16.6 | 3.231 | 2.942 | 1.782 |
| 2b | 58.4 | -4.9 | 2.991 | 2.891 | 1.922 |
| 3 | -79.7 | 8.8 | 1.933 | 2.439 | 3.173 |
| | NEVPT2 | | | | |
| | D_{cal} | E_{cal} | g_x | g_y | g_z |
| 1a | 52.6 | 12.3 | 2.990 | 2.771 | 1.959 |
| 1b | 52.0 | 5.8 | 2.920 | 2.818 | 1.970 |
| 2a | 53.8 | 9.8 | 2.960 | 2.760 | 1.967 |
| 2b | 51.4 | 4.1 | 2.873 | 2.798 | 1.986 |
| 3 | -67.7 | 4.5 | 1.956 | 2.514 | 3.094 |

To deeply analyze their magnetic anisotropies, we have obtained the principal contributions of the excited states (with relative energy, cm^{-1}) to D values for **1–3** using NEVPT2 with ORCA 4.2, which are listed in Table S10†. The origin of positive D values of **1** and **2** come mainly from the first and second quartet excited states while the negative sign of **3** is mainly determined by the first and third quartet excited states.

In order to get further insight into the electronic structures caused by the different axial ligands in **1–3**, the relative energy order (cm^{-1}) of ligand field d-orbitals splitting for complexes **1–3** have been extracted according to AI-LFT (AILFT) analysis using NEVPT2 implemented in ORCA 4.2. (Table S11, ESI†).^{83–84} The d-orbital diagram for the ground state of **1–3** are shown in Fig. S28†. It is found that the ground states of **1–3** are multideterminant, which suggests the strong spin-orbit coupling in **1–3**. In both **1** and **2**, the singly occupied $d_{x^2-y^2}$ state exhibits the strongest destabilization from the ligand field while d_{xy} is the most stable. Further, the other one doubly occupied and two singly occupied states are very close in energy and act as linear combination of d_{xz} , d_{yz} and d_z^2 AOs, which might be the cause for the multideterminant character for the ground states of **1–2**. In contrast with **1** and **2**, the most destabilized state is dominated by d_z^2 and the d_{yz} is lowest in energy. The differences between **1** or **2** and **3** is caused by the nature of axial ligands (weak Cl^- or Br^- in **1** and **2** vs strong NCO^- in **3**). This suggests that the various axial ligand would give the different ground and excited states, which give the different nature of magnetic anisotropies for this series of five-coordinate Co(II) complexes. The calculated orientations of the g_x , g_y and g_z in the ground spin-orbit states on Co^{II} ions of complexes **1–3** (Fig. S29†) are different. In **1** and **2**, the g_z orientation (hard axis) lies along the $\text{Co-X}_{\text{axial}}$ bond while the g_x orientation (easy axis) is nearly perpendicular to the $\text{Co-N}_{\text{axial}}$ bond in **3**.

As reported earlier, we introduced the more rigid 12-membered tetraazamacrocyclic ligand 12-TMC to construct the CH_3CN -coordinated complexes $[(12\text{-TMC})\text{Co}(\text{CH}_3\text{CN})]^{2+}$, with a ground spin state with $S = 1/2$, which exhibits field-induced SIM behavior at low temperature.⁵⁶ Then a high-spin complex $[\text{Co}(12\text{-TMC})(\text{NCO})][\text{B}(\text{C}_6\text{H}_5)_4]$ (**3**) with NCO^- as the axial ligand was found to

exhibit an easy-axis magnetic anisotropy.⁵⁷ In the present work, with further changing the axial ligand to halide such as Cl^- and Br^- , positive anisotropy was found for **1** and **2**. Since the tetragonal-pyramidal configuration of these four complexes with 12-TMC are stable with similarly small τ^5 values, they allow us to examine the influence of the axial ligand on the magnetic anisotropy in the tetragonal-pyramidal complexes. Our comparative studies could lead to the following important conclusion: the employment of the weak halide ligand would give the easy-plane magnetic anisotropy in contrast with strong negative anisotropy induced by a strong axial NCO^- ligand.

Conclusions

In summary, we synthesized two five-coordinate mononuclear Co(II) complexes **1** and **2** utilizing a rigid tetradentate macrocyclic ligand 12-TMC and investigated the magnetic anisotropy and slow magnetic dynamics. The X-ray single-crystal diffraction analyses show similar square pyramidal configuration in **1** and **2**. Their positive magnetic anisotropies have been revealed by magnetometry, HF-EPR and theoretical calculations. The ac susceptibility studies demonstrate that **1** and **2** exhibit slow magnetic relaxation behavior under the applied dc fields. Compared with the reported easy-axis magnetic anisotropy for the analogue complex **3** with a strong terminal ligand NCO^- , the positive anisotropy in **1** and **2** could be due to the terminal weak ligands. These studies clearly show that the variation of terminal ligand is an effective approach to fine-tune the magnetic properties of in the square pyramidal Co(II) complexes.

Conflicts of interest

There are no conflicts to declare.

Acknowledgements

We are grateful for the financial support from the Natural Science Grant of China (No. 21471078 to XTC and 21973046 to YQZ) and the US National Science Foundation (CHE-1633870 and CHE-1900296 to ZLX).

Notes and references

- D. Gatteschi, R. Sessoli, and J. Villain, *Molecular Nanomagnets*; Oxford University Press: Oxford, UK, 2006.
- R. Bagai and G. Christou, *Chem. Soc. Rev.*, 2009, **38**, 1011–1026.
- K. S. Pedersen, J. Bendix and R. Clérac, *Chem. Commun.*, 2014, **50**, 4396–4415.
- W. Wernsdorfer and R. Sessoli, *Science*, 1999, **284**, 133–135.
- M. N. Leuenberger and D. Loss, *Nature*, 2001, **410**, 789–793.
- M. Affronte, *J. Mater. Chem.*, 2009, **19**, 1730–1737.
- N. Ishikawa, M. Sugita, T. Ishikawa, S.-Y. Koshihara, Y. Kaizu, *J. Am. Chem. Soc.* 2003, **125**, 8694–8695.
- D. N. Woodruff, R. E. P. Winpenny and R. A. Layfield, *Chem. Rev.*, 2013, **113**, 5110–5148.

- 9 J. M. Frost, K. L. M. Harriman and M. Murugesu, *Chem. Sci.*, 2016, **7**, 2470–2491.
- 10 G. A. Craig and M. Murrie, *Chem. Soc. Rev.*, 2015, **44**, 2135–2147.
- 11 A. K. Bar, C. Pichon and J.-P. Sutter, *Coord. Chem. Rev.*, 2016, **308**, 346–380.
- 12 S. Tripathi, A. Dey, M. Shanmugam, R. S. Narayanan, and V. Chandrasekhar, *Top. Organomet. Chem.*, 2019, **64**, 35–76.
- 13 M. Murrie, *Chem. Soc. Rev.*, 2010, **39**, 1986–1995.
- 14 Rechkemmer, Y.; Breitgoff, F. D.; van der Meer, M.; Atanasov, M.; Haki, M.; Orlita, M.; Neugebauer, P.; Neese, F.; Sarkar, B. and van Slageren, *J. Nat. Commun.* 2016, **7**, 10467(1–8).
- 15 H.-H. Cui, F. Lu, X.-T. Chen, Y.-Q. Zhang, W. Tong and Z.-L. Xue, *Inorg. Chem.*, 2019, **58**, 12555–12564.
- 16 S. Tripathi, S. Vaidya, K. U. Ansari, N. Ahmed, E. Rivière, L. Spillecke, C. Koo, R. Klingeler, T. Mallah, G. Rajaraman, and M. Shanmugam, *Inorg. Chem.*, 2019, **58**, 9085–9100.
- 17 S. Vaidya, P. Shukla, S. Tripathi, E. Rivière, T. Mallah, G. Rajaraman, and M. Shanmugam, *Inorg. Chem.*, 2018, **57**, 3371–3386.
- 18 J. Vallejo, I. Castro, R. Ruiz-García, J. Cano, M. Julve, F. Lloret, G. De Munno, W. Wernsdorfer, E. Pardo, *J. Am. Chem. Soc.* 2012, **134**, 15704–15707.
- 19 Y. -Y. Zhu, C. Cui, Y. -Q. Zhang, J. -H. Jia, X. Guo, C. Gao, K. Qian, S. -D. Jiang, B. -W. Wang, Z. -M. Wang, S. Gao, *Chem. Sci.* 2013, **4**, 1802–1806.
- 20 F. Habib, O. R. Luca, V. Vieru, M. Shiddiq, I. Korobkov, S. I. Gorelsky, M. K. Takase, L. F. Chibotaru, S. Hill, R. H. Crabtree and M. Murugesu, *Angew. Chem. Int. Ed.*, 2013, **52**, 11290–11293.
- 21 R. F. Higgins, B. N. Livesay, T. J. Ozumerzifon, J. P. Joyce, A. K. Rappé and M. P. Shores, *Polyhedron*, 2018, **143**, 193–200.
- 22 T. Jurca, A. Farghal, P.-H. Lin, I. Korobkov, M. Murugesu, and D. S. Richeson, *J. Am. Chem. Soc.*, 2011, **133**, 15814–15817.
- 23 J.-J. Liu, Y.-S. Meng, I. Hlavička, M. Orlita, S.-D. Jiang, B.-W. Wang and S. Gao, *Dalton Trans.*, 2017, **46**, 7408–7411.
- 24 I. Nemeč, H. Liu, R. Herchel, X. Zhang and Z. Trávníček, *Syn. Metal.*, 2016, **215**, 158–163.
- 25 A. K. Mondal, T. Goswami, A. Misra and S. Konar, *Inorg. Chem.*, 2017, **56**, 6870–6878.
- 26 C. Rajnák, F. Varga, J. Titiš, J. Moncol and R. Boča, *Eur. J. Inorg. Chem.*, 2017, 1915–1922.
- 27 B. Brachňaková, S. Matejová, J. Moncol, R. Herchel, J. Pavlik, E. Moreno-Pineda, M. Ruben and I. Šalitraš, *Dalton Trans.*, 2020, **49**, 1249–1264.
- 28 A. Świtlicka, B. Machura, M. Penkala, A. Bieńko, D. C. Bieńko, J. Titiš, C. Rajnák, R. Boča, A. Ozarowski and M. Ozerov, *Inorg. Chem.*, 2018, **57**, 12740–12755.
- 29 C. Rajnák, J. Titiš, O. Fuhr, M. Ruben and R. Boča, *Inorg. Chem.*, 2014, **53**, 8200–8202.
- 30 C. Rajnák, J. Titiš, J. Miklovič, G. E. Kostakis, O. Fuhr, M. Ruben and R. Boča, *Polyhedron*, 2017, **126**, 174–183.
- 31 Y. Cui, Y. Xu, X. Liu, Y. Li, B.-L. Wang, Y. Dong, W. Li and S. Lei, *Chem. Asian J.*, 2019, **14**, 2620–2628.
- 32 Y. Cui, Y. Ge, Y. Li, J. Yao and Y. Dong, *Struct. Chem.*, DOI: 10.1007/s11224-019-01429-3.
- 33 I. Nemeč, R. Herchel and Z. Trávníček, *Dalton Trans.*, 2016, **45**, 12479–12482.
- 34 J. Acharya, A. Sarkar, P. Kumar, V. Kumar, J. F. Gonzalez, O. Cadon, F. Pointillart, G. Rajaraman and V. Chandrasekhar, *Dalton Trans.*, 2020, **49**, 4785–4796.
- 35 I. Banerjee, A. Jana, S. Singh, J. Marek, E. del Barco, M. Ali, *Polyhedron*, 2013, **66**, 162–166.
- 36 D. M. Piñero Cruz, D. N. Woodruff, I.-R. Jeon, I. Bhowmick, M. Secu, E. A. Hillard, P. Dechambenoit and R. Clérac, *New J. Chem.*, 2014, **38**, 3443–3448.
- 37 A. Packová, J. Miklovič and R. Boča, *Polyhedron*, 2015, **102**, 88–93.
- 38 R. Ruamps, L. J. Batchelor, R. Guillot, G. Zakhia, A.-L. Barra, W. Wernsdorfer, N. Guihéry and T. Mallah, *Chem. Sci.*, 2014, **5**, 3418–3424.
- 39 K. A. Schulte, K. R. Vignesh and K. R. Dunbar, *Chem. Sci.*, 2018, **9**, 9018–9026.
- 40 F. Shao, B. Cahier, N. Guihéry, E. Rivière, R. Guillot, A.-L. Barra, Y. Lan, W. Wernsdorfer, V. E. Campbell and T. Mallah, *Chem. Commun.*, 2015, **51**, 16475–16478.
- 41 F. Shao, B. Cahier, Y.-T. Wang, F.-L. Yang, E. Rivière, R. Guillot, N. Guihéry, J.-P. Tong, and T. Mallah, *Chem. Asian J.*, 2020, **15**, 391–397.
- 42 F. Shao, B. Cahier, E. Rivière, R. Guillot, N. Guihéry, V. E. Campbell and T. Mallah, *Inorg. Chem.*, 2017, **56**, 1104–1111.
- 43 D. Schweinfurth, M. G. Sommer, M. Atanasov, S. Demeshko, S. Hohloch, F. Meyer, F. Neese and B. Sarkar, *J. Am. Chem. Soc.*, 2015, **137**, 1993–2005.
- 44 A. K. Mondal, J. Jover, E. Ruiz and S. Konar, *Chem. Eur. J.*, 2017, **23**, 12550–12558.
- 45 T. J. Woods, M. F. Ballesteros-Rivas, S. Gómez-Coca, E. Ruiz and K. R. Dunbar, *J. Am. Chem. Soc.*, 2016, **138**, 16407–16416.
- 46 F. El-Khatib, B. Cahier, F. Shao, M. López-Jordà, R. Guillot, E. Rivière, H. Hafez, Z. Saad, J.-J. Girerd, N. Guihéry and T. Mallah, *Inorg. Chem.*, 2017, **56**, 4601–4608.
- 47 A. Collet, G. A. Craig, M. J. H. Ojea, L. Bhaskaran, C. Wilson, S. Hill and M. Murrie, *Dalton Trans.*, 2018, **47**, 9237–9240.
- 48 M. A. Hay, A. Sarkar, G. A. Craig, L. Bhaskaran, J. Nehr Korn, M. Ozerov, K. E. R. Marriott, C. Wilson, G. Rajaraman, S. Hill and M. Murrie, *Chem. Sci.*, 2019, **10**, 6354–6361.
- 49 N. Nedelko, A. Kornowicz, I. Justyniak, P. Aleshkevych, D. Prochowicz, P. Krupiński, O. Dorosh, A. Ślawska-Waniewska, and J. Lewiński, *Inorg. Chem.*, 2014, **53**, 12870–12876.
- 50 I. Nemeč, R. Marx, R. Herchel, P. Neugebauer, J. van Slagerenb and Z. Trávníček, *Dalton Trans.*, 2015, **44**, 15014–15021.
- 51 X. Hou, X. Wang, X. Liu, J. Wang, L. Tang and P. Ju, *New J. Chem.*, 2018, **42**, 8583–8590.
- 52 A. K. Mondal, J. Jover, E. Ruiz and S. Konar, *Chem. Commun.*, 2017, **53**, 5338–5341.
- 53 A. K. Mondal, J. Jover, E. Ruiz and S. Konar, *Dalton Trans.*, 2019, **48**, 25–29.
- 54 S. Mandal, S. Mondal, C. Rajnák, J. Titiš, R. Boča and S. Mohanta, *Dalton Trans.*, 2017, **46**, 13135–13144.
- 55 A. K. Mondal, A. Mondal and S. Konar, *Magnetochemistry*, 2019, **5**, 12(1–11).
- 56 H.-H. Cui, J. Wang, X.-T. Chen and Z.-L. Xue, *Chem. Commun.*, 2017, **53**, 9304–9307.
- 57 H.-H. Cui, Y.-Q. Zhang, X.-T. Chen, Z. Wang and Z.-L. Xue, *Dalton Trans.*, 2019, **48**, 10743–10752.
- 58 A. W. Addison, T. N. Rao, J. Reedijk, J. Vanrijn and G. C. Verschoor, *J. Chem. Soc., Dalton Trans.*, 1984, 1349–1356.
- 59 M. Llnell, D. Casanova, J. Cirera, P. Alemany and S. Alvarez, *Shape Program*, Version 2.1, 2013.
- 60 S. Alvarez, P. Alemany, D. Casanova, J. Cirera, M. Llnell and D. Avnir, *Coord. Chem. Rev.*, 2005, **249**, 1693–1708.
- 61 J. Cho, R. Sarangi, H. Y. Kang, J. Y. Lee, M. Kubo, T. Ogura, E. I. Solomon and W. Nam, *J. Am. Chem. Soc.*, 2010, **132**, 16977–16986.
- 62 SMART & SAINT Software Reference Manuals, version 6.45; Bruker Analytical X-ray Systems, Inc.: Madison, WI, 2003.
- 63 SAINT, Program for Data Extraction and Reduction, Siemens Analytical X-ray Instruments, Madison, WI, 1994–1996.
- 64 G. M. Sheldrick, SADABS: Software for Empirical Absorption Correction, version 2.05; University of Göttingen: Göttingen, Germany, 2002.
- 65 G. M. Sheldrick, SHELXL14: Program for Crystal Structure Refinement; University of Göttingen: Göttingen, Germany, 2014.

- 66 G. A. Bain and J. F. Berry, *J. Chem. Educ.*, 2008, **85**, 532–536.
- 67 S. L. Wang, L. Li, Z. W. Ouyang, Z. C. Xia, N. M. Xia, T. Peng and K. B. Zhang, *Acta Phys. Sin.*, 2012, **61**, 107601(1–5).
- 68 H. Nojiri and Z. W. Ouyang, *Terahertz Sci. Technol.*, 2012, **5**, 1–10.
- 69 N. F. Chilton, R. P. Anderson, L. D. Turner, A. Soncini and K. S. Murray, *J. Comput. Chem.*, 2013, **34**, 1164–1175.
- 70 Simulations were performed using SPIN developed by Andrew Ozarowski of the National High Magnetic Field Laboratory, USA.
- 71 F. R. Xavier, A. Neves, A. Casellato, R. A. Peralta, A. J. Bortoluzzi, B. Szpoganicz, P. C. Severino, H. Terenzi, Z. Tomkowicz, S. Ostrovsky, W. Haase, A. Ozarowski, J. Krzystek, J. Telsler, G. Schenk and L. R. Gahan, *Inorg. Chem.*, 2009, **48**, 7905–7921;
- 72 L. Banci, A. Bencibini, C. Benelli, D. Gatteschi and C. Zanchini, *Struct. Bonding*, 1982, **52**, 37–86.
- 73 E. Y. Misochko, A. V. Akimov, D. V. Korchagin, J. Nehr Korn, M. Ozerov, A. V. Palii, J. M. Clemente-Juan and S. M. Aldoshin, *Inorg. Chem.*, 2019, **58**, 16434–16441.
- 74 J. R. Pilbrow, *J. Magn. Reson.*, 1978, **31**, 479–490.
- 75 M. T. Werth, S.-F. Tang, G. Formicka, M. Zeppezauer and M. K. Johnson, *Inorg. Chem.*, 1995, **34**, 218–228.
- 76 F. Neese, E. I. Solomon in *Magnetism: Molecules to Materials*, Vol. IV (Eds.: J. S. Miller, M. Drillon), Wiley-VCH, Weinheim, 2002.
- 77 K. S. Cole and R. H. Cole, *J. Chem. Phys.*, 1941, **9**, 341–351;
- 78 Y.-N. Guo, G.-F. Xu, Y. Guo and J. Tang, *Dalton Trans.*, 2011, **40**, 9953–9963.
- 79 F. Aquilante, J. Autschbach, R. K. Carlson, L. F. Chibotaru, M. G. Delcey, L. De Vico, I. Fdez. Galván, N. Ferré, L. M. Frutos, L. Gagliardi, M. Garavelli, A. Giussani, C. E. Hoyer, G. Li Manni, H. Lischka, D. Ma, P. Å. Malmqvist, T. Müller, A. Nenov, M. Olivucci, T. B. Pedersen, D. Peng, F. Plasser, B. Pritchard, M. Reiher, I. Rivalta, I. Schapiro, J. Segarra-Martí, M. Stenrup, D. G. Truhlar, L. Ungur, A. Valentini, S. Vancoillie, V. Veryazov, V. P. Vysotskiy, O. Weingart, F. Zapata, R. Lindh, *J. Comput. Chem.*, 2016, **37**, 506–541.
- 80 F. Neese, *ORCA—an ab initio, density functional and semiempirical program package*, Version 4.2; Max-Planck institute for bioinorganic chemistry: Mülheim an der Ruhr, Germany, **2019**.
- 81 Y.-Z. Zhang, S. Gómez-Coca, A. J. Brown, M. R. Saber, X. Zhang and K. R. Dunbar, *Chem. Sci.*, 2016, **7**, 6519–6527.
- 82 P. Konieczny, A. B. Gonzalez-Guillén, K. Luberda-Durnaś, E. Čížmár, R. Peřka, M. Oszejca and W. Łasořha, *Dalton Trans.*, 2019, **48**, 7560–7570.
- 83 M. Atanasov, D. Ganyushin, K. Sivalingam and F. Neese, *Struct. Bond.*, 2012, **143**, 149–220.
- 84 S. K. Singh, J. Eng, M. Atanasov and F. Neese, *Coord. Chem. Rev.*, 2017, **344**, 2–25.

Magnetic anisotropy in square-pyramidal cobalt(II) complexes supported by a tetraazomacrocyclic ligand

Hui-Hui Cui, Man-Man Ding, Xiu-Du Zhang, Wei Lv, Yi-Quan Zhang, Xue-Tai Chen, Zhenxing Wang, Zhong-Wen Ouyang and Zi-Ling Xue

Positive magnetic anisotropies of two square-pyramidal cobalt(II) complexes have been revealed by magnetic measurements, HF-EPR spectroscopy and theoretical calculations.

